Core–Shell Bimetallic Carbide Nanoparticles Confined in a Three-Dimensional N-Doped Carbon Conductive Network for Efficient Lithium Storage

Ying Xiao, Pingping Sun, and Minhua Cao*

Key Laboratory of Cluster Science, Ministry of Education of China, Beijing Key Laboratory of Photoelectronic/Electrophotonic Conversion Materials, Department of Chemistry, Beijing Institute of Technology, Beijing 100081, P. R. China

ABSTRACT Carbides represent a class of functional materials with unique properties and increasing importance. However, the harsh conditions in conventional synthetic strategies impede subtle control over size and morphology of carbides, which is highly imperative for their practical applications. Herein, we report a facile, simple approach to prepare porous Co_3ZnC/N-doped carbon hybrid nanospheres. In this structure, the Co_3ZnC nanoparticles exhibit a core–shell structure and they are uniformly confined in N-doped carbon conductive networks forming rather uniform nanospheres. The hybrid nanospheres have a specific surface area as high as 170.5 $m^2\ g^{-1}$. When evaluated as an anode material for lithium ion batteries, they show an excellent lithium storage performance, which can be attributed to the combined effect of the core–shell Co_3ZnC nanoparticles, the pore structure and the highly conductive and elastic N-doped carbon networks. This work provides an efficient route for the facile production of nanoscale carbides with desirable manipulation over size and morphology for many of important applications.

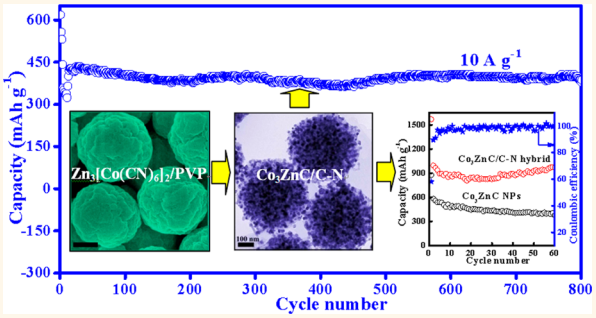

KEYWORDS: Co_3ZnC · N-doped carbon · core–shell · anode materials · lithium ion batteries

Transition-metal carbides (TMCs) have been known since the pioneering work of Levy and Boudart in 1973,[1] and they have recently received renewed research interest. In terms of their structure, TMCs possess simple metallic structures with small carbon atoms in the interstitial voids of the densely packed host lattice, which therefore are classified into the family of interstitial alloys (the inset in Figure 1a).[2] Because of their special structure, they show an unusual combination of outstanding properties, such as high melting point, high electrical and thermal conductivities, exceptional hardness, excellent mechanical stability, and chemical stability along with the resistance against corrosion under reaction conditions.[3,4] This combination of these properties has attracted considerable attention and has led to numerous technical applications and theoretical investigations.[4–11] Several recent reports on TMCs mainly focused on their catalytic and electrochemical applications. For instance, Hou *et al.* reported a facile bromide-induced synthesis of Fe_5C_2 nanoparticles (NPs),[12] which could be used as a catalyst for Fischer–Tropsch synthesis. Molybdenum carbides (MoC) have been applied in both the catalytic synthesis and decomposition of NH_3.[13] Shen *et al.* demonstrated nanosized tungsten carbides (WC) for high-performance electrocatalysis.[14] Just recently, nevertheless, Gogotsi *et al.* demonstrated by combining density functional theory (DFT) calculations and experiments that two-dimensional layered carbides, such as Nb_2C, V_2C, Cr_2C, Ti_2C, and so on, are promising electrode materials for lithium ion batteries (LIBs), and the lithiation and delithiation mechanisms were

* Address correspondence to caomh@bit.edu.cn.

Received for review March 11, 2014 and accepted August 3, 2014.

Published online August 03, 2014
10.1021/nn501390j

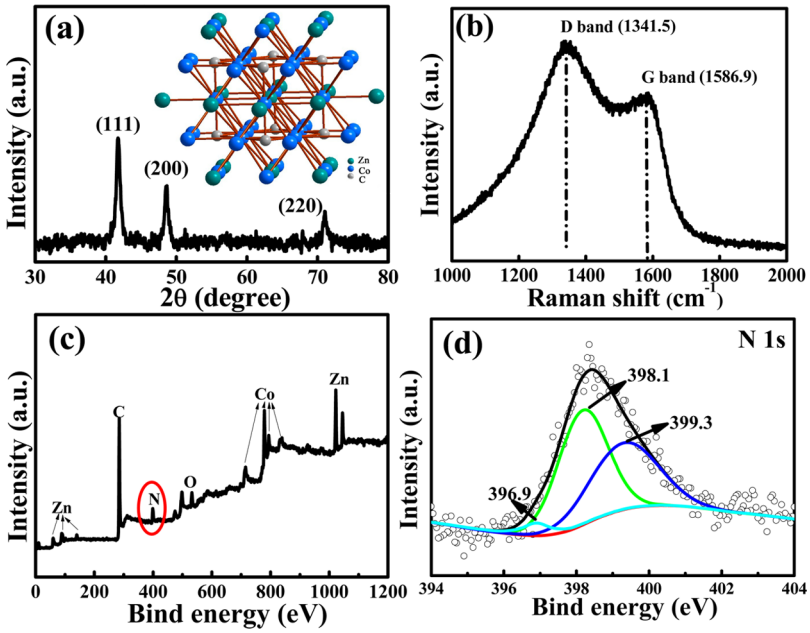

Figure 1. (a, b) XRD pattern and Raman spectrum of the $Co_3ZnC/C-N$ hybrid (inset: crystal structure of Co_3ZnC); (c) survey XPS spectrum of the $Co_3ZnC/C-N$ hybrid; (d) high-resolution XPS spectrum of N 1s.

found to be Li intercalation and deintercalation between the layers.[4,7,8,10,15] In addition, Zhou *et al.* investigated the electronic properties and Li storage capability of Ti_3C_2 in detail also by density DFT computations. The results showed that Ti_3C_2 possesses some exceptional properties, including good electronic conductivity, fast Li ion diffusion, low operating voltage, and high theoretical Li storage capacity,[3] all of which make it an ideal anode for LIBs. Inspired by the above studies and considering that Zn, Ti, or Co elements are relatively low cost, highly natural abundance, and environmental benignity compared to Mo, Nb, V, or Cr, in this report, we, for the first time, demonstrate lithium storage performance of bimetallic carbide—Co_3ZnC as an anode in LIBs by experimental investigation.

As is well known, the ability to control particle size and morphology is an important objective in the synthesis of nanostructured materials, as the size and shape can significantly influence various properties. For example, the particle size can greatly affect their surface area, while the high surface area is of particular importance regarding, for example, electrode reactions, because of the increase of interaction of the active materials of the electrode with electrolyte. However, the traditional metallurgy techniques for the synthesis of TMCs involve reaction of the metals with carbon at high temperatures, and the resultant TMCs are mainly limited to irregular particles with relative large size (several microns) and low surface area (6.7—108 $m^2\ g^{-1}$).[12,16,17] Therefore, to obtain TMCs as nanoscale materials with well-defined shape, size, and composition, traditional solid-state synthesis based on the reaction of powder precursors is unsuitable. In view of this situation, several approaches subsequently were developed for synthesizing TMCs with nanoscale particle size and high surface area, mainly including soft/hard template method,[18] high-temperature decomposition,[19] carbothermal reduction, or temperature-programmed reduction.[20,21] Although these methods deliver a relatively high surface area compared to the traditional ones, the obtained TMCs still cannot meet the requirements of some high-performance applications. The lack of efficient control over the particle size and morphology is a serious problem for further development of nanoscale TMCs.

Furthermore, it has been well addressed that materials with nanoscale particle size often display relatively high activity originating from the intrinsic properties of nanomaterials, such as high surface area and high surface energy. Therefore, nanomaterials are inherently vulnerable to oxidation or agglomeration, thus leading to the decreasing of the final performance.[22,23] Therefore, compositing nanoscale TMCs with carbon may be an alternative means to alleviate this problem, and the carbon existing in the composites can provide the oxidation resistance and avoid the agglomeration of the bare NPs. Until now, there have been several reports on the compositing of TMCs with carbon, which has proved highly effective in improving the studied performance. For example, Zhao *et al.* reported the ordered mesoporous TiC/C composites using a self-assembly approach, in which the highly dispersed TiC NPs embedded in the matrix of amorphous carbon show significant property enhancement;[24] Feng *et al.* synthesized core—shell structured Fe/Fe_3C-C nanorods, which exhibit excellent performance as advanced electrocatalysts for oxygen reduction reaction.[25]

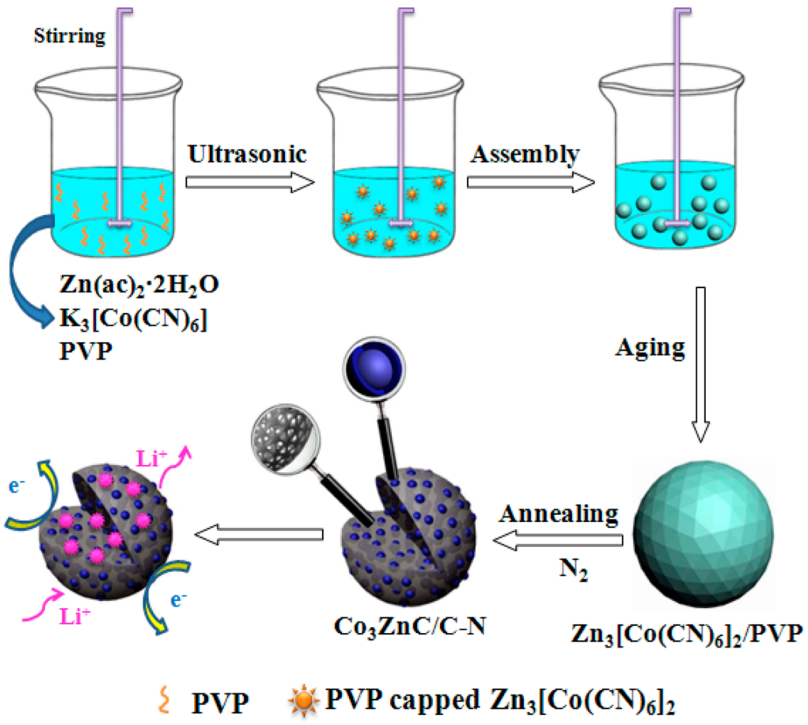

Scheme 1. Schematic Illustration of the Fabrication of $Co_3ZnC/C-N$ Hybrid and Its Application in LIBs

Additionally, several other TMCs/C nanocomposites have also been reported in different fields such as LIBs, dye-sensitized solar cells, methanol oxidation, and so on.[26−31]

Herein, we for the first time propose a facile strategy for fabricating Co_3ZnC core−shell NPs embedded in three-dimensional (3D) porous N-doped carbon conductive networks ($Co_3ZnC/C-N$ hybrid) *via* a facile ultrasonic method followed by annealing treatment. The $Co_3ZnC/C-N$ hybrid shows a hierarchically porous structure with specific surface area as high as 170.5 $m^2\ g^{-1}$. When evaluated as an anode for LIBs, the $Co_3ZnC/C-N$ hybrid exhibits higher specific capacity and significantly enhanced cycling performance compared to Co_3ZnC NPs.

RESULTS AND DISCUSSION

The schematic illustration for the fabrication of the Co_3ZnC core−shell NPs embedded in 3D N-doped carbon conductive networks is shown in Scheme 1. First, the preparation of uniform $Zn_3[Co(CN)_6]_2$/polyvinylpyrrolidone (PVP) ($Zn_3[Co(CN)_6]_2$/PVP) nanospheres is based on our previous work *via* an ultrasonic method in the presence of PVP (see Figure S1, Supporting Information).[32] The subsequent annealing treatment at 600 °C converts the $Zn_3[Co(CN)_6]_2$/PVP precursor into a $Co_3ZnC/C-N$ hybrid, and in this process the spherical morphology of the precursor is well maintained. The crystalline composition of the annealed sample can be identified as the cubic Co_3ZnC phase (JCPDS card No. 29-0524) by X-ray diffraction (XRD) analysis (Figure 1a), and the Co_3ZnC displays a typical alloy structure (the inset in Figure 1a). The average crystalline size of the Co_3ZnC particles was determined to be about 15.3 nm based on the Scherrer formula. Here, it should be pointed out that if the annealing temperature is higher or lower than 600 °C, for example, 500 or 700 °C, a pure Co_3ZnC phase cannot be obtained (Figure S2a, Supporting Information). The possible reason may be ascribed to the insufficient energy for the formation of the pure Co_3ZnC phase at the lower temperature and the volatilization of Zn component at the higher temperature.[33] Moreover, we also tried lower pressures still at 600 °C, and similarly, we still did not obtain a pure Co_3ZnC phase (Figure S2b, Supporting Information), which may be because the lower pressure increases the volatile rate of the components and thus decreases their residence time in the solid particles, leading to the formation of different phases in the final product.[34] The above experimental results indicate that the annealing temperature and pressure in our case are particularly important for the formation of pure Co_3ZnC phase from the thermal transformation of the $Zn_3[Co(CN)_6]_2$/PVP precursor.

The chemical composition of the sample annealed at 600 °C was further investigated by Raman and X-ray photoelectron spectroscopy (XPS) measurements (Figure 1b−d and Figure S3 in the Supporting Information). Figure 1b shows the Raman spectrum of the sample, which presents two strong peaks at 1341.5 and 1586.9 cm^{-1} in the range of 1000−2000 cm^{-1}, which can be assigned to typical D and G bands of the carbon materials, respectively. This result suggests the

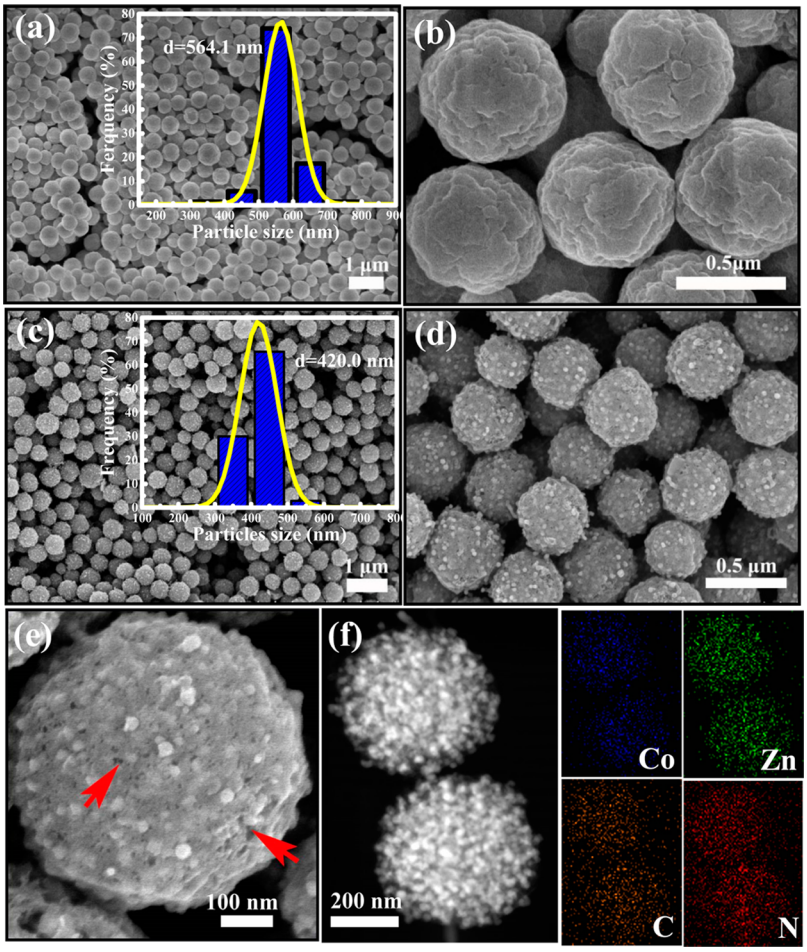

Figure 2. FE-SEM images of (a, b) the precursor; (c–e) the $Co_3ZnC/C-N$ hybrid; (f) STEM image and the corresponding element mapping images. The profiles in a and c show the corresponding particle size distribution.

existence of carbon in this sample. The N-doping was ascertained by survey spectrum and high resolution N 1s spectrum (Figure 1c,d) (here it should be noted that we performed the XPS measurement on a sputtered surface in order to get the substantial information on the sample, not just the very outer surface). As shown in Figure 1d, the N 1s peak can be deconvoluted into three components with binding energies at 399.3, 398.1, and 396.9 eV, which can be assigned to pyrrolic nitrogen, pyridinic nitrogen, and nitrogen atoms bonded to Zn or Co atoms, respectively.

$Zn_3[Co(CN)_6]_2$/PVP nanospheres prepared *via* an ultrasonic method were used as the precursor. The low-magnification field emission scanning electron microscopy (FE-SEM) image (Figure 2a) showed that the precursor was composed of highly uniform spheres with an average diameter of ca. 564.1 nm (inset in Figure 2a). A high-magnification FE-SEM image (Figure 2b) revealed that the surface of the sphere is very rough, suggesting that the spheres may be assembled from smaller subunits. More interestingly, after being annealed at 600 °C for 2 h, the resultant $Co_3ZnC/C-N$ still maintains the spherical morphology of the precursor, and the very uniform spheres have an average diameter of about 420.0 nm (Figure 2c), which is smaller than that of the precursor, suggesting that an obvious shrinkage occurs during this annealing process. Unlike the rough surface of the precursor, the surface of the $Co_3ZnC/C-N$ sample is embedded with many NPs, as shown in the high-magnification FE-SEM image (Figure 2d). A magnified FE-SEM image of an individual nanosphere could more clearly display the details of the sphere, as shown in Figure 2e. In fact, the NPs composed of the sphere are cross-linked with 3D porous networks, which are similar to the structure of the sponge, and the pores can be clearly observed (marked by red arrows). Furthermore, the element mapping images obtained by X-ray energy dispersive spectroscopy (EDS) attached with an electron microscope (STEM) confirm the presence of Zn, Co, C, and N elements, in agreement with Raman and XPS results, and that these elements were uniformly distributed through the whole nanospheres (Figure 2f). The CHN element analysis reveals that the $Co_3ZnC/C-N$ sample contains 31.2 wt % carbon and 8.69 wt % nitrogen. The mass concentration of Co and Zn by ICP-MS measurement was determined to be 39.7 and 21.9 μg mL^{-1}, respectively, and thus, the C weight percentage in the

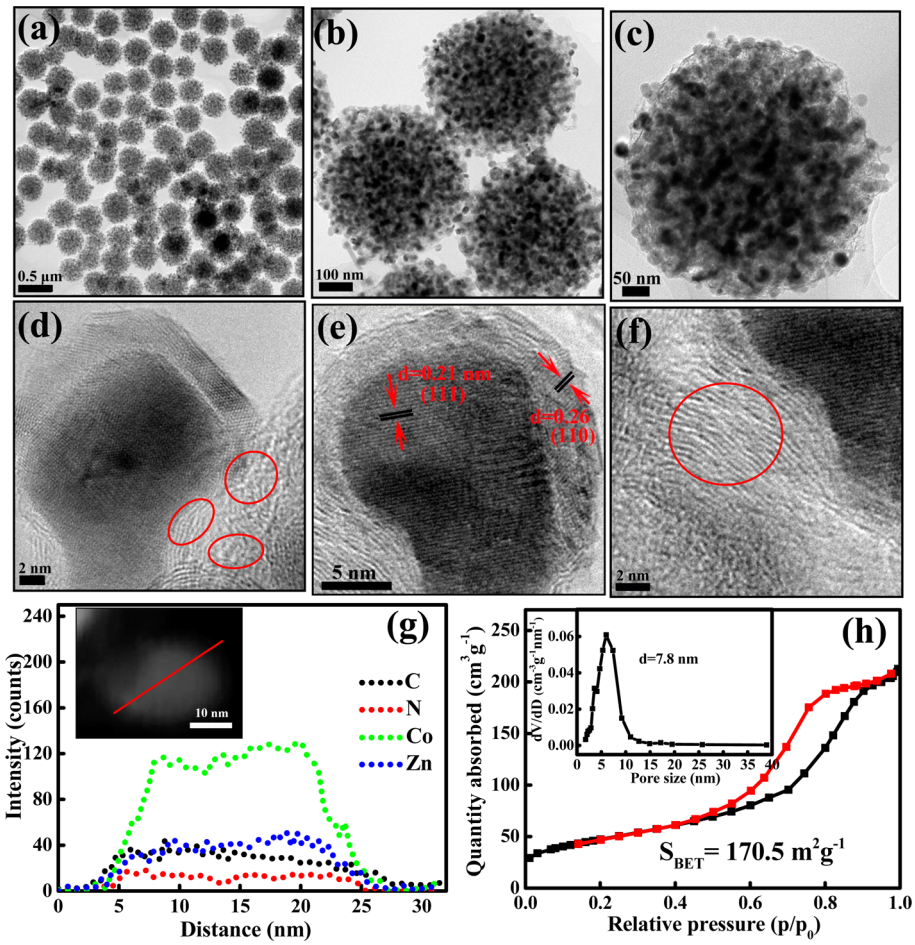

Figure 3. (a–c) TEM images of the Co_3ZnC/C–N hybrid at different magnifications; (d–f) representative HRTEM images; (g) STEM image (the inset one) and the corresponding cross-sectional compositional line profiles; (h) nitrogen adsorption–desorption isotherms and pore size distribution curves of the Co_3ZnC/C–N hybrid.

Co_3ZnC is calculated to be 4.06 wt % on the basis of the ICP result of Zn. Combining this result with the elemental analysis, the free carbon composited with Co_3ZnC is calculated to be 27.1 wt %. According to all these measurements (XRD, element analysis, element mapping, Raman, and XPS), we affirmatively deduce that the annealed sample is a hybrid of Co_3ZnC and N-doped carbon (named as Co_3ZnC/C–N), in which the NPs are Co_3ZnC, while the 3D porous networks are N-doped carbon.

The microstructure of the Co_3ZnC/C–N hybrid was further investigated by transmission electron microscopy (TEM). Figure 3a,b display the typical TEM images of this hybrid, indicating the well-defined uniform nanospheres, which is consistent with SEM result. These spheres exhibit excellent dispersibility with diameter of about 420 nm. Figure 3c shows a TEM image of an individual sphere, from which it can be clearly seen that darker Co_3ZnC NPs with diameter of about 15–20 nm are embedded in gray 3D N-doped carbon networks, which have a very loose structure. It is more interesting to note that the Co_3ZnC NPs actually possess a core–shell structure, as shown in the high-resolution TEM images of single particle (Figure 3d,e). The interplane spaces in the shell and core are calculated to be 0.26 and 0.21 nm (Figure 3e), which agree well with the (110) and (111) lattice planes of cubic Co_3ZnC, respectively, further confirming that the core and shell both belong to Co_3ZnC phase. More importantly, it can be clearly seen from Figure 3d–f that the core–shell Co_3ZnC NPs are firmly wrapped by thin onion- like carbon shells (marked by red circles), indicating the strong interaction between Co_3ZnC and carbon. This interaction could effectively prevent Co_3ZnC NPs from falling off the carbon networks during discharge/charge process, thus ensuring the stable performance of the hybrid. In order to further verify the core–shell structure of the Co_3ZnC NPs, STEM measurement was carried out. Figure S4a,b in the Supporting Information shows the annular bright-field (BF)- and dark-field (DF)-STEM images for one particle, from which an obvious contrast between the core and the shell can be detected. An element mapping investigation (Figure S4b, Supporting Information) and the line profiles across one particle (Figure 3g) also revealed that the core and shell are same component. In addition, the micro-EDS spectra recorded from different positions of one particle

further suggested that the core and the shell of the particle both are composed of Co_3ZnC, and the Co_3ZnC NPs are distributed in the N-doped C networks (Figure S5, Supporting Information). The texture and porosity of the precursor and $Co_3ZnC/C-N$ hybrid are characterized by measuring N_2 adsorption–desorption isotherms (Figure S6, Supporting Information and Figure 3h). From the isotherms we can see that the $Co_3ZnC/C-N$ hybrid shows a hierarchical micro-mesopore structure with an average pore diameter of about 7.8 nm and a Brunauer–Emmett–Teller (BET) surface area as high as 170.5 $m^2 g^{-1}$. The pore diameter is much larger than that of the precursor (2.7 nm), while the surface area is obviously lower than that of the precursor (536.4 $m^2 g^{-1}$). This result reflects that this annealing process was accompanied by a change in terms of the phase and microstructure. It should be noted that the large pore diameter and the relatively high surface area for the annealed sample will be beneficial for its storage performance because the electrolyte can be penetrated completely into the pores, leading to a higher electrolyte/electrode contact area and more facile adsorption for Li ions on the NPs and within the pores.[35−39]

Furthermore, a $Zn_3[Co(CN)_6]_2$ precursor instead of $Zn_3[Co(CN)_6]_2$/PVP can be obtained if no PVP was used in the preparing process. Figure S7 (Supporting Information) shows FT-IR spectra of these two precursors obtained with and without PVP addition. It can be clearly seen that the obvious peaks at about 2185.5 and 472.6 cm^{-1} in both spectra can be assigned to C–N and Co–CN, respectively. However, compared with that of the $Zn_3[Co(CN)_6]_2$, the FT-IR spectrum of the $Zn_3[Co(CN)_6]_2$/PVP exhibits some new peaks at about 2957.9, 1291.0, 666.2 cm^{-1}, which can be attributed to PVP, indicating the adsorption of PVP on the surface of the $Zn_3[Co(CN)_6]_2$. The presence of PVP not only can effectively avoid the aggregation of Co_3ZnC NPs but also is beneficial for the formation of the 3D carbon network. Figure S8a (Supporting Information) shows a SEM image of the as-obtained $Zn_3[Co(CN)_6]_2$ precursor, from which it can be seen that the $Zn_3[Co(CN)_6]_2$ sample consists of regular polyhedrons with a larger size. After annealing, the $Zn_3[Co(CN)_6]_2$ polyhedrons were crushed into small particles (Figure S8b, Supporting Information), which can be determined to be pure Co_3ZnC phase by XRD pattern (Figure S8c, Supporting Information). The TEM image, the STEM image, the corresponding cross-sectional compositional line profiles along with the element mapping images, and the micro-EDS spectra are also provided to further reveal the composition and the element distribution of this sample (Figure S8d–k, Supporting Information). These results indicate the important role of PVP in the formatting of 3D spherical network. We define this sample as Co_3ZnC NPs and in the following study it serves as a control sample.

Considering its unique nanostructure and special composition, the resultant $Co_3ZnC/C-N$ hybrid is believed to have potential application as an anode material in LIBs. Hence, we for the first time investigated its Li storage performance. Figure 4a displays the discharge/charge voltage profiles of the $Co_3ZnC/C-N$ hybrid cycled at a current density of 0.1 A g^{-1} in a potential window of 0.01–3 V (vs Li^+/Li). The initial discharge and charge-specific capacities are 1570.1 and 911.3 mA h g^{-1}, respectively. Although a large irreversible capacity loss is observed in the first cycle, the reversible capacity is still as high as 995.6 mA h g^{-1} in the second cycle and could be maintained up to 968.1 mA h g^{-1} in the 60th cycle, indicating the excellent reversibility of this material. The irreversible capacity loss in the first cycle can be partly attributed to the formation of solid electrolyte interphase (SEI) film on the surface of the electrode.[36−40] This result is also in good agreement with that from the cyclic voltammetry (CV) curves, which show an obvious reduction peak in the potential of 0.65 V only in the first cycle (Figure 4b). Like the reported studies, the former is related to the irreversible reactions between the electrode and electrolyte, and the latter is due to the electrolyte decomposition and the formation of the SEI film.[24,37] In the subsequent cycles, no evident redox peaks were observed, from which it can be preliminarily deduced that the Co_3ZnC material does not follow the conventional conversion reaction mechanism.

To further investigate its Li storage mechanism, the XPS spectra of Zn and Co of the $Co_3ZnC/C-N$ electrode after cycling at different states were performed. As shown in Figure 4c, the Co 2p spectrum after discharged to 0.01 V can be fitted to 777.8, 778.9, 780.8, 783.9, 792.9, 794.5, 796.9, and 803.1 eV. The strongest peak at 777.8 eV as well as the one at 792.9 eV can be assigned to Co^0. The peak at 778.9 eV can be assigned to the Co $2p_{3/2}$ of Co^{2+} with the shakeup satellite at 783.9 eV, while the one at 794.5 eV is due to the Co $2p_{1/2}$ with the satellite peak at 803.1 eV. The other two weak peaks are related to Co^{3+}. However, for the case after charged to 3 V, the Co 2p spectrum displays almost similar curve to that after discharged to 0.01 V with respect to peak number and peak position. Thus, it can be seen that the oxidation state of Co has no change during above discharge/charge process. Similarly, for the Zn 2p XPS spectrum, it shows two evident peaks at about 1021.2 and 1044.2 eV for the one after discharged to 0.01 V; after charged to 3 V, the peaks at about 1020.9 and 1043.9 eV are obtained. Compared with those before cycling (1021.7 and 1044.8 eV) (Figure S3, Supporting Information), a little change of the peak position is generated, which may be induced by the change of the local environment. From the XPS results we can see that no valence state change for Co_3ZnC is observed during the discharging/charging process. In addition, an examination of the XRD

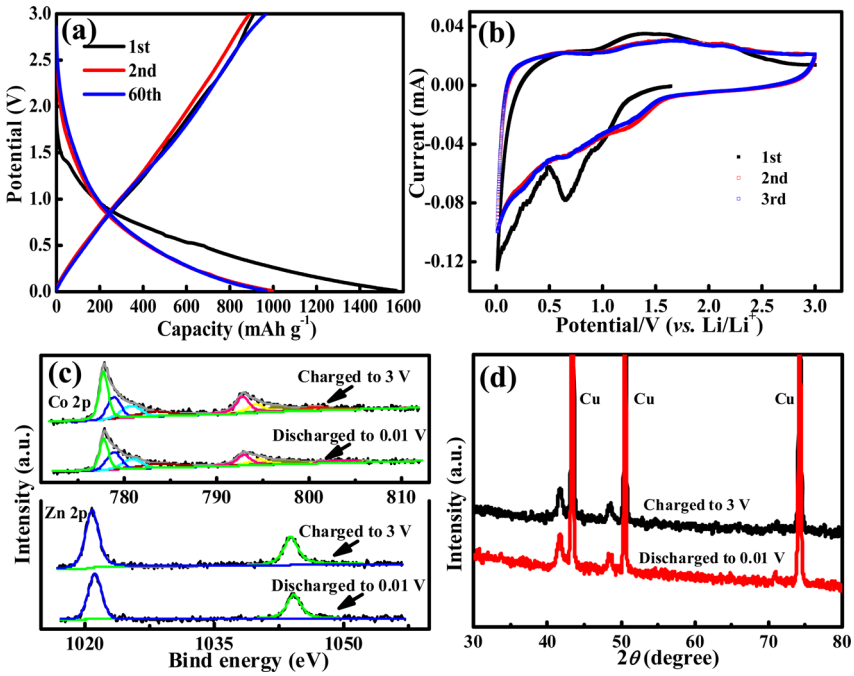

Figure 4. (a) Charge−discharge profiles of Co_3ZnC/C−N hybrid for the first, second, and 60th cycles at a current density of 0.1 A g^{-1}. (b) CV curves for the as-resultant hybrid at a scan rate of 0.1 mV s^{-1}. (c) The comparison of Zn 2p and Co 2p XPS spectra of the as-prepared Co_3ZnC/C−N spheres after four cycles: charged to 3 V and discharged to 0.01 V, respectively. (d) XRD patterns of the Co_3ZnC/C−N electrode after four cycles.

patterns during the cycling process shows that no extra peaks appear (Figure 4d); only the diffraction peaks of the Co_3ZnC phase have a slight downshift. By the XRD rietveld refinement, the lattice parameters are determined to be 0.3758 nm (after discharged to 0.01 V) and 0.3750 nm (after charged to 3 V) after 4 discharge/charge processes, respectively, whereas that before cycling is 0.3738 nm. Thus, the lattice parameter changes only in the range of 0.3%−0.5% during the discharging/charging process. These XPS and XRD analyses further confirm aforementioned deduction; i.e., it is not the conversion reaction.

Furthermore, from the lattice parameter changes we also know that such a small volume expansion is obviously inconsistent with the high Li storage capacity obtained from above experimental results if the Li storage mechanism is Li intercalation. Actually, we have also confirmed this fact by *ab initio* calculations based on density functional theory (DFT). The favorable sites with different Li concentrations, and the corresponding coordinates are provided in Figure S9 and Tables S1 and S2 (Supporting Information). It can be seen that even if 0.5 Li is intercalated into one Co_3ZnC unit cell, the volume expansion is as least 11.6% but still keeping the initial crystal structure. However, 1 Li per one Co_3ZnC unit cell leads to volume expansion as high as 25.3% and near-destruction of the initial crystal structure. It should be noted that such a large volume expansion (25.3%) is also highly inconsistent with previous lattice parameter changes. In fact, the Li intercalated numbers that correspond to the reversible charge capacity (968.1 mA h g^{-1} for the 60th cycle) obtained experimentally are much more than 1 Li/one Co_3ZnC unit cell. Therefore, these contradictory results strongly suggest that other Li storage models excluding the conversion reaction and the Li intercalation mechanism should be taken into consideration for good Li storage properties. According to recently reported studies,[41,42] Li can adsorb on the surface of NPs and fill into the interspersed pores to achieve Li storage. Therefore, in our case, the hierarchical micro/mesopores, the small-size core−shell Co_3ZnC NPs, and 3D N-doped carbon conductive network can serve as reservoirs for Li storage, and all these factors contributed to the excellent Li storage performance of the resultant hybrid system.

Figure 5a shows the galvanostatic cycling performance of the Co_3ZnC/C−N hybrid together with its Coulombic efficiency at a current density of 0.1 A g^{-1}. It is interesting to observe that the discharge capacity decreases slightly before 20 cycles and then gradually increases to 968.1 mAh g^{-1}. This value is 2.6 times the theoretical capacity of commercial graphite (372 mAh g^{-1}). According to the literature,[36,43−45] the reason for the change trend of the capacity can be probably attributed to two aspects: the gradual penetration of electrolyte into the inner of the porous active materials during cycling at a low current density and the progressive generation of electrochemistry active polymeric films. During the tested 60 cycles, although the initial Coulombic efficiency is only 58.1% for the first cycle, it increases sharply to the 89.5% during the

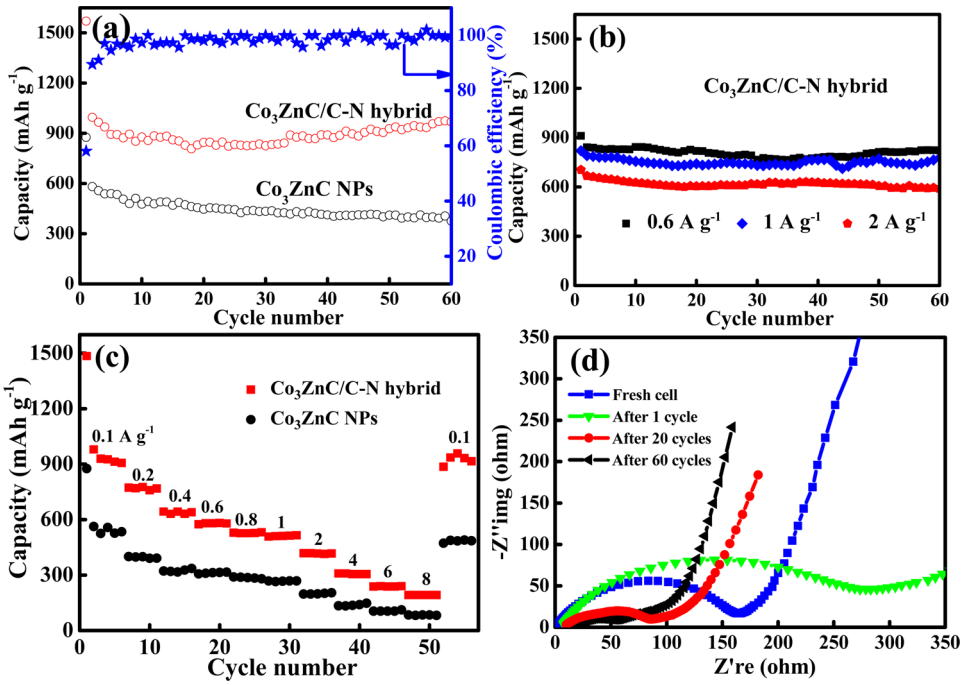

Figure 5. Electrochemical properties of the as-prepared electrodes for Li storage: (a) cycling performance of $Co_3ZnC/C-N$ and Co_3ZnC NPs electrodes at a current density of 0.1 A g^{-1} and coulombic efficiency of $Co_3ZnC/C-N$ at a current density of 0.1 A g^{-1}; (b) cycling performance of $Co_3ZnC/C-N$ electrode at different current densities; (c) rate performance at varied current densities from 0.1 to 8 A g^{-1}; (d) electrochemical impedance spectroscopies of the $Co_3ZnC/C-N$ electrode tested before cell testing, after 1 cycle, 20 cycles, and 60 cycles at a current density of 0.1 A g^{-1}.

second cycle and reaches over 98.0% after the 15th cycle. This value can be maintained in the subsequent cycles, indicating excellent cycling stability of this material. Furthermore, more importantly, the $Co_3ZnC/C-N$ hybrid also displays outstanding cycling performance at larger current densities. As shown in Figure 5b, the electrode can deliver specific capacity of 820.6, 767.6, and 589.7 mA h g^{-1} at 0.6, 1, and 2 A g^{-1} after 60 cycles, respectively, and under all tested conditions, they all exhibit perfect cycling stability. As is well known, the rate capability plays a significant role in many applications such as electric vehicles and portable power tools. Therefore, we also investigate the rate performance of the materials at various current densities (from 0.1 to 8 A g^{-1}), and the results are presented in Figure 5c. It should be noted that when the current density is returned to 0.1 A g^{-1}, the capacity can recover to the original value, indicating the excellent capacity capability of the $Co_3ZnC/C-N$ hybrid. However, for Co_3ZnC NPs, they exhibit lower capacity and poorer cycling performance compared to the $Co_3ZnC/C-N$ hybrid (Figure 5a,c). This may be related to its composition and structure. In detail, for the 3D $Co_3ZnC/C-N$ hybrid, the N-doping could induce more active sites for the additional Li storage,[43,45] while the highly conductive N-doped carbon networks possess high mechanical stability and could maintain the integrity of the electrode during cycling, thus ensuring the excellent stability performance.[46] Furthermore, to further understand the excellent performance of Li storage of the $Co_3ZnC/C-N$ hybrid, electrochemical impedance spectroscopy (EIS) measurements were carried out after different cycles of discharging/recharging at 0.1 A g^{-1}. As clearly seen in Figure 5d, the impedance of a fresh cell is smaller than that of the first cycle, indicating the formation of SEI film after the first cycle, which is common in most anode materials.[38,39,43,44] However, in contrast to most reports that the cell impedance increases with increasing cycle numbers, the cell impedance decreases obviously with increasing cycle numbers, indicating the smaller impedance of the $Co_3ZnC/C-N$ hybrid electrode with the cycle increase. This phenomenon may be associated with its 3D N-doped carbon networks. In order to further expound this issue, the electrochemical impedance spectroscopies of the 3D $Co_3ZnC/C-N$ hybrid after different cycles were fitted on the basis of the equivalent circuit model (Figure S10, Supporting Information). The fitted results indicate that the charge transfer resistances (Rct) of $Co_3ZnC/C-N$ hybrid at the 1st, 20th, and 60th cycles are 244.1, 81.4, and 43.2 Ω, respectively, displaying a significant decrease of Rct with cycling. This result is similar to those in previous literature and may be ascribed to the existence of the activating process and the wetting of the electrode materials with the electrolyte in the porous structure and the 3D carbon matrix.[47−50] Moreover, with the increase of the cycle number, the SEI film resistances (R_{SEI}) of the $Co_3ZnC/C-N$ for the 1st, 20th, and 60th cycles at 0.1 A g^{-1} are

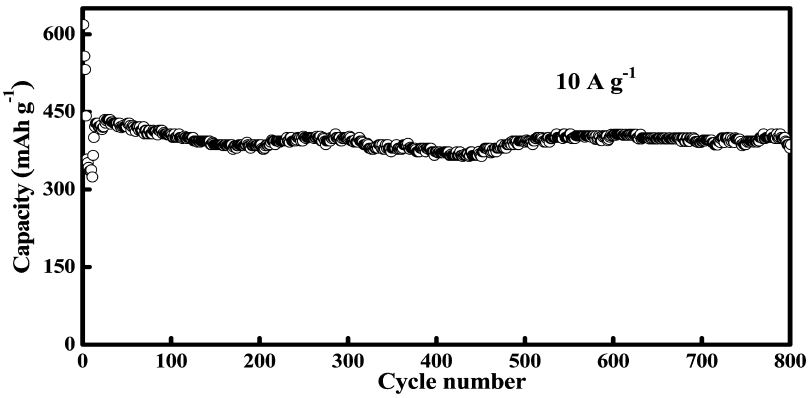

Figure 6. Cycling performance of $Co_3ZnC/C-N$ hybrid at 10 A g^{-1} for 800 cycles.

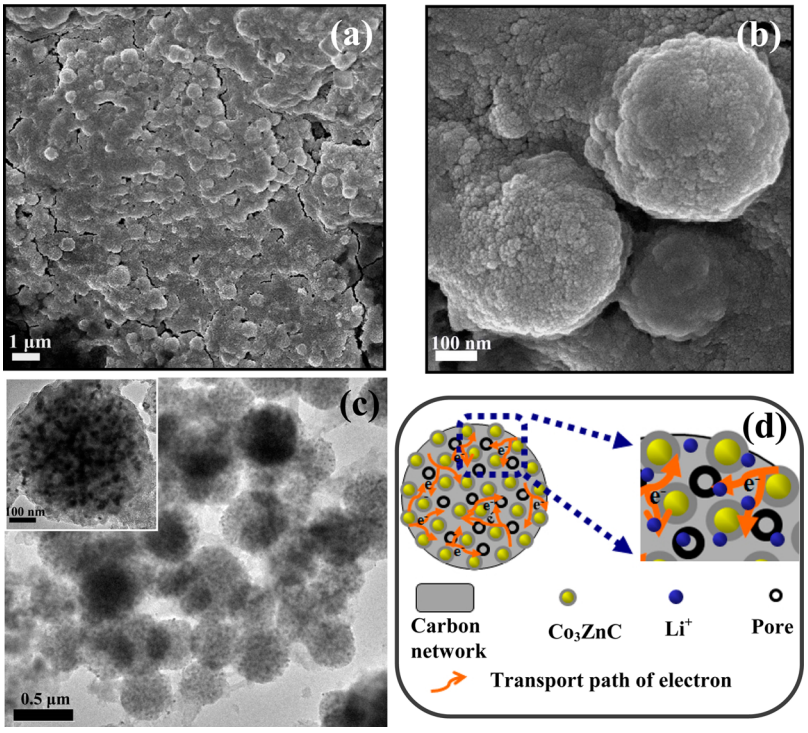

Figure 7. SEM images of the $Co_3ZnC/C-N$ electrode after cycled for 60 cycles at a current density of 0.1 A g^{-1}: (a) low magnification; (b) high magnification; (c) TEM image of the $Co_3ZnC/C-N$ electrode after cycled for 60 cycles at a current density of 0.1 A g^{-1} and inset is TEM image of a single nanosphere; (d) schematic illustration of discharging/charging mechanism for the $Co_3ZnC/C-N$ hybrid.

determined to be 33.0, 31.2, and 30.5 Ω, respectively, which are far lower than those (134.6, 130.0, and 56.9 Ω) of the Co_3ZnC NPs. More importantly, compared to Co_3ZnC NPs, the 3D $Co_3ZnC/C-N$ hybrid has R_{SEI} values at different cycles with a slight change, indicating a more stable SEI film. We deduce that it is the 3D N-doped carbon network that plays a key role in stabilizing the SEI film.[47,51]

We believe that the superior performance of the $Co_3ZnC/C-N$ hybrid is closely related to its unique structure. Even at a higher current density of 10 A g^{-1}, corresponding to a time of 5 min to finish a discharge/charge process, the $Co_3ZnC/C-N$ electrode still delivers a capacity of as high as 386.6 mAh g^{-1} after the 800th cycle (Figure 6), which is still higher than the theoretical capacity of graphite (372 mA h g^{-1}). To further confirm excellent stability of this structure, we tested the morphology of the $Co_3ZnC/C-N$ hybrid after 60 cycles at a current density of 0.1 A g^{-1}. TEM and SEM examinations for the electrode reveal that after 60 cycles the spherical morphology of the $Co_3ZnC/C-N$ hybrid is perfectly retained, and moreover, no Co_3ZnC NPs fall off the hybrid spheres (Figure 7a–c), confirming the superior structural stability. This superior stability can be ascribed to the elastic carbon 3D conductive networks as well as their close wrapping for the core–shell Co_3ZnC NPs, which could provide the mechanical/structure integrity during cycling. To the best of our knowledge, this is the first report on the Li storage application for $Co_3ZnC/C-N$

hybrid, and its excellent Li storage performance demonstrates the great potential as a promising high rate anode material in LIBs.

The excellent electrochemical performance of the $Co_3ZnC/C-N$ hybrid could be attributed to its unique composition and microstructure, which feature the following advantages (Figure 7d): (1) the hierachically microporous-mesoporous structure may act as a reservoir for storage of Li^+, and it is beneficial to the easy immersion and diffusion of the electrolyte, which can provide short path lengths with less resistance for both Li ion and electron transport within electrolyte;[38,39,43−45,52,53] (2) the N-doping can introduce more active sites for the additional Li storage; (3) the highly conductive N-doped carbon network not only could provide a continuous pathway for electron transport and Li^+ diffusion but also could effectively stabilize the as-formed SEI films;[54−56] (4) the small-sized core−shell Co_3ZnC NPs in the $Co_3ZnC/C-N$ hybrid is beneficial for adsorbing more Li on their surface due to their high activity. All of these factors are responsible for the excellent Li storage performance of the $Co_3ZnC/C-N$ hybrid.

CONCLUSIONS

In summary, we have demonstrated a facile and effective path to synthesize a porous $Co_3ZnC/C-N$ hybrid. In this structure, core−shell Co_3ZnC NPs were uniformly embedded in N-doped carbon conductive networks to form rather uniform nanospheres. The $Co_3ZnC/C-N$ hybrid was formed by thermally induced reduced decomposition of $Zn_3[Co(CN)_6]_2$/PVP nanospheres at 600 °C in a N_2 atmosphere. When evaluated as an anode material for LIBs. The novel hybrid material presents a remarkable Li storage performance, capacity retention, and rate capability. The outstanding performance is mainly attributed to the porous structure, highly conducting carbon networks, and small core−shell Co_3ZnC NPs. Furthermore, this strategy for constructing this unique structure and special composition would be very helpful in boosting the electrochemical performance of other nanomaterials.

METHODS

Synthesis of $Co_3ZnC/C-N$. All of the reagents used are of analytical purity and used without further purification. In a typical precursor, the $Zn_3[Co(CN)_6]_2$/PVP was first synthesized by a ultrasonic method according to the literature with little modification. Two solutions were prepared. Solution A: 0.132 g of $Zn(ac)_2 \cdot 2H_2O$ and 1.112 g of PVP (K30) were dissolved in 20 mL of destilled water under magnetic stirring to form a transparent solution. Solution B: 0.133 g $K_3[Co(CN)_6]$ was dissolved in 20 mL of distilled water with stirring. Then the solution B was slowly added into solution A dropwise under agitated stirring and ultrasonic radiation in an ice−water bath. After reaction for 20 min, the reaction mixture was further maintained for 1 h, and subsequently the reaction was aged at room temperature for 24 h. Finally, the obtained product was washed with distilled water several times. After freeze-drying for 24 h, the $Zn_3[Co(CN)_6]_2$/PVP was annealed at 600 °C under atmospheric pressure for 2 h at N_2 atmosphere with a heating rate of 3 °C/min to yield the final product.

Characterization. The obtained products were characterized on an powder X-ray diffraction (XRD) (Bruker D8 X-ray power diffactometer) operated at 40 kV voltage and 50 mA current. An XRD pattern was recorded from 30 to 80° (2θ) with a scanning step of 5°/min. The morphologies of the resulting products were examined by a H-8100 transmission electron microscopy (TEM) operating at 200 kV accelerating voltage and field emission scanning electron microscopy (FE-SEM). The EDS element mapping images of the sample were acquired by using a scanning transmission electron microscope (STEM) (FEI Technai G2 F20) operating at 200 kV. BF- and HAADF images were taken with a JEOL 2010F microscope in STEM mode with the use of the BF- and HAADF detector. The microanalysis of EDS spectra were also taken with a JEOL 2010F microscope. X-ray photoelectron spectra (XPS) were recorded on an ESCALAB 250 spectrometer (Perkin Elmer) to characterize the chemical composition of the $Co_3ZnC/C-N$ hybrid and the electrodes after discharging/charging. The XPS measurement was conducted with sputtering for 360 s with an air-ion beam operating at 3 kV and 3 μA. High-resolution spectra were carried out with the pass energy of 20 eV and the energy step of 0.1 eV. For the testing of the materials after cycling, the cell was disassembled, and the electrode was taken out. The electrode was washed by dimethyl carbonate (DEC) and then dried at the vacuum condition. Finally, the materials were peeled off from the Cu foil for further XPS measurement. The carbon content was determined by an elemental analyzer (Vario EI) using combustion method. Inductively coupled plasma spectrometry (ICP) was carried out on a Jarrel-ASH (ICAP-9000). Raman spectra were recorded on an Invia Raman spectrometer, with an excitation laser wavelength of 514.5 nm. The Brunauer−Emmett−Teller (BET) surface area of as-synthesized samples was measured using a Belsorp-max surface area detecting instrument by N_2 physisorption at 77 K.

Electrochemical Measurements. The electrochemical behavior of the obtained products was examined by coin-type cells (2025) assembled in an argon filled glovebox. The working electrode was obtained by mixture of active material, carbon black, and polyvinylidene fluoride (PVDF) binder with a weight ratio of 80:10:10 onto a copper foil current collector. The typical electrode was dried at 120 °C for 24 h under vacuum before being assembled into a coin cell in an argon-filled glovebox. A Celgard 2400 microporous polypropylene membrane was used as the separator, and Li foil was used as the counter electrode. The nonaqueous electrolyte used was 1 M $LiPF_6$ dissolved in an ethylene carbonate (EC)/dimethyl carbonate (DMC)/diethyl carbonate (DEC) mixture (1:1:1, in vol %). Galvanostatic cycling experiments of the cells were performed on a LAND CT2001A battery test system in the voltage range of 0.01−3 V *versus* Li^+/Li at room temperature. Cyclic voltammetry (CV) curves were recorded on a CHI-760E workstation at a scanning rate of 0.1 mV s^{-1}. The impedance spectra of the cell were measured by applying a sine wave with amplitude of 5 mV over the frequency range from 100 kHz to 0.01 Hz.

Conflict of Interest: The authors declare no competing financial interest.

Supporting Information Available: Characterization of the precursor including TEM image, the XRD pattern, and the BET plot; high-resolution XPS spectra of Zn, Co, and C; XRD patterns of the products obtained at different pressures and different temperatures; BF-STEM images, STEM of one particle, and the corresponding element mapping of each element, TEM image of one particle, and the corresponding EDS spectra selected from different area; FT-IR spectra of the PVP, the precursor prepared without the addition of PVP, and the precursor prepared with the addition of PVP; characterization for the sample obtained without PVP including the SEM image, XRD pattern, TEM image, STEM image, and the corresponding element

mapping along with the EDS spectra; detailed information about the *ab initio* calculations based on the density functional theory (DFT); electrochemical impedance spectroscopies of the electrode and the simulated results of the electrode. This material is available free of charge *via* the Internet at http://pubs.acs.org.

Acknowledgment. This work was financially supported by the National Natural Science Foundation of China (Nos. 21271023, 91022006, and 20973023) and the 111 Project (B07012).

REFERENCES AND NOTES

1. Levy, R. B.; Boudart, M. Platinum-Like Behavior of Tungsten Carbide in Surface Catalysis. *Science* **1973**, *181*, 547–549.
2. Lengauer, W. Transition Metal Carbides, Nitrides, and Carbonitrides. In *Handbook of Ceramic Hard Materials*, 1st ed.; Riedel, R., ed.; Wiley-VCH: Weinheim, Germany, 2000.
3. Tang, Q.; Zhou, Z.; Shen, P. W. Are MXenes Promising Anode Materials for Li Ion Batteries? Computational Studies on Electronic Properties and Li Storage Capability of Ti_3C_2 and $Ti_3C_2X_2$ (X= F, OH) Monolayer. *J. Am. Chem. Soc.* **2012**, *134*, 16909–16916.
4. Naguib, M.; Halim, J.; Lu, J.; Cook, K. M.; Hultman, L.; Gogotsi, Y.; Barsoum, M. W. New Two-Dimensional Niobium and Vanadium Carbides as Promising Materials for Li-Ion Batteries. *J. Am. Chem. Soc.* **2013**, *135*, 15966–15969.
5. Sun, Z. M. Progress in Research and Development on MAX Phases—A Family of Metallic Ceramics. *Int. Mater. Rev.* **2011**, *56*, 143–166.
6. Wang, X. H.; Zhou, Y. C. Layered Machinable and Electrically Conductive Ti_2AlC and Ti_3AlC_2 Ceramics: a Review. *J. Mater. Sci. Technol.* **2010**, *26*, 385–412.
7. Lukatskaya, M. R.; Mashtalir, O.; Ren, C. E.; Dall'Agnese, Y.; Rozier, P.; Taberna, P. L.; Naguib, M.; Simon, P.; Barsoum, M. W.; Gogotsi, Y. Cation Intercalation and High Volumetric Capacitance of Two-Dimensional Titanium Carbide. *Science* **2013**, *341*, 1502–1505.
8. Mashtalir, O.; Naguib, M.; Mochalin, V. N.; Dall'Agnese, Y.; Heon, M.; Barsoum, M. W.; Gogotsi, Y. Intercalation and Delamination of Layered Carbides and Carbonitrides. *Nat. Commun.* **2013**, *4*, 1716–1722.
9. Gao, Q.; Zhao, X. Y.; Xiao, Y.; Zhao, D.; Cao, M. H. A Mild Route to Mesoporous Mo_2C/C Hybrid Nanospheres for High Performance Lithium-Ion Batteries. *Nanoscale* **2014**, *6*, 6151–6157.
10. Come, J.; Naguib, M.; Rozier, P.; Barsoum, M. W.; Gogotsi, Y.; Taberna, P. L.; Morcrette, M.; Simon, P. A Non-Aqueous Asymmetric Cell with a Ti_2C-Based Two-Dimensional Negative Electrode. *J. Electrochem. Soc.* **2012**, *159*, A1368–A1373.
11. Xie, Y.; Nagui, M.; Mochalin, V. N.; Barsoum, M. W.; Gogotsi, Y.; Yu, X. Q.; Nam, K. W.; Yang, X. Q.; Kolesnikov, A. I.; Kent, P. R. C. Role of Surface Structure on Li-Ion Energy Storage Capacity of Two-Dimensional Transition-Metal Carbides. *J. Am. Chem. Soc.* **2014**, *136*, 6385–6394.
12. Yang, C.; Zhao, H. B.; Hou, Y. L.; Ma, D. Fe_5C_2 Nanoparticles: A Facile Bromide-Induced Synthesis and as an Active Phase for Fischer—Tropsch Synthesis. *J. Am. Chem. Soc.* **2012**, *134*, 15814–15821.
13. Zheng, W. Q.; Cotter, T. P.; Kaghazchi, P.; Jacob, T.; Frank, B.; Schlichte, K.; Zhang, W.; Su, D. S.; Schüth, F.; Schlögl, R. Experimental and Theoretical Investigation of Molybdenum Carbide and Nitride as Catalysts for Ammonia Decomposition. *J. Am. Chem. Soc.* **2013**, *135*, 3458–3464.
14. Yan, Z. X.; Cai, M.; Shen, P. K. Nanosized Tungsten Carbide Synthesized by a Novel Route at Low Temperature for High Performance Electrocatalysis. *Sci. Rep.* **2013**, *3*, 1646–1652.
15. Naguib, M.; Come, J.; Dyatkin, B.; Presser, V.; Taberna, P. L.; Simon, P.; Barsoum, M. W.; Gogotsi, Y. MXene: A Promising Transition Metal Carbide Anode for Lithium-Ion Batteries. *Electrochem. Commun.* **2012**, *16*, 61–64.
16. Hanif, A.; Xiao, T.; York, A. P. E.; Sloan, J.; Green, M. L. H. Study on the Structure and Formation Mechanism of Molybdenum Carbides. *Chem. Mater.* **2002**, *14*, 1009–1015.
17. Myers, W. R.; Fishel, W. P. The Preparation and Hydrolysis of Manganese Carbide (Mn_3C). *J. Am. Chem. Soc.* **1945**, *67*, 1962–1964.
18. Lunkenbein, T.; Rosenthal, D.; Otremba, T.; Girgsdies, F.; Li, Z.; Sai, H.; Bojer, C.; Auffermann, G.; Wiesner, U.; Breu, J. Access to Ordered Porous Molybdenum Oxycarbide/Carbon Nanocomposites. *Angew. Chem., Int. Ed.* **2012**, *51*, 12892–12896.
19. Preiss, H.; Meyer, B.; Oschewski, C. Preparation of Molybdenum and Tungsten Carbides from Solution Derived Precursors. *J. Mater. Sci.* **1998**, *33*, 713–722.
20. Ledoux, M. J.; Hantzer, S.; Huu, C. P.; Guille, J.; Desaneaux, M. P. New Synthesis and Uses of High-Specific-Surface SiC as a Catalytic Support That It Is Chemically Inert and Has High Thermal Resistance. *J. Catal.* **1988**, *114*, 176–185.
21. Lee, J. S.; Volpe, L.; Riberio, F. H.; Boudart, M. Molybdenum Carbide Catalysts: II. Topotactic Synthesis of Unsupported Powders. *J. Catal.* **1988**, *112*, 44–53.
22. Li, R.; Zhang, P.; Huang, Y. H.; Zhang, P.; Zhong, H.; Chen, Q. W. Pd-Fe_3O_4@C Hybrid Nanoparticles: Preparation, Characteriaztion, and Their High Catalytic Activity toward Suzuki Coupling Rections. *J. Mater. Chem.* **2012**, *22*, 22750–22755.
23. Zhu, M. Y.; Diao, G. W. Magnetically Recyclable Pd Nanoparticles Immobilized on Magnetic Fe_3O_4@C Nanocomposites: Preparation, Characterization, and Their Catalytic Activity toward Suzuki and Heck Coupling Reactions. *J. Phys. Chem. C* **2011**, *115*, 24743–24749.
24. Yu, T.; Deng, Y. H.; Wang, L.; Liu, R. L.; Zhang, L. J.; Tu, B.; Zhao, D. Y. Ordered Mesoporous Nanocrystalline Titanium-Carbide/Carbon Composites from *in Situ* Carbothermal Reduction. *Adv. Mater.* **2007**, *19*, 2301–2306.
25. Wen, Z. H.; Ci, S. Q.; Zhang, F.; Feng, X. L.; Cui, S. M.; Mao, S.; Luo, S. L.; He, Z.; Chen, J. H. Nitrogen-Enriched Core-Shell Structured Fe/Fe_3C-C Nanorods as Advanced Electrocatalysts for Oxygen Reduction Reaction. *Adv. Mater.* **2012**, *24*, 1399–1404.
26. Song, H.; Chen, X. Large-Scale Synthesis of Carbon-Encapsulated Iron Carbide Nanoparticles by Co-Carbonization of Durene with Ferrocene. *Chem. Phys. Lett.* **2003**, *374*, 400–404.
27. Voevodin, A. A.; Prasad, S. V.; Zabinski, J. S. Nanocrystalline Carbide/Amorphous Carbon Composites. *J. Appl. Phys.* **1997**, *82*, 855–858.
28. Zhao, X. Y.; Xia, D. G.; Yue, J. C.; Liu, S. Z. *In-Situ* Generated Nano-Fe_3C Embedded into Nitrogen-Doped Carbon for High Performance Anode in Lithium Ion Battery. *Electrochim. Acta* **2014**, *116*, 292–299.
29. Liao, Y. P.; Pan, K.; Wang, L.; Pan, Q. J.; Zhou, W.; Miao, X. H.; Jiang, B. J.; Tian, C. G.; Tian, G. H.; Wang, G. F.; Fu, H. G. Facile Synthesis of High-Crystallinity Graphitic Carbon/Fe_3C Nanocomposites as Counter Electrodes for High-Efficiency Dye-Sensitized Solar Cells. *ACS Appl. Mater. Interfaces* **2013**, *5*, 3663–3670.
30. Su, L. W.; Zhou, Z.; Shen, P. W. Core-Shell Fe@Fe_3C/C Nanocomposites as Anode Materials for Li Ion Batteries. *Electrochim. Acta* **2013**, *87*, 180–185.
31. Lu, J. L.; Li, Z. H.; Jiang, S. P.; Shen, P. K.; Li, L. Nanostructured Tungsten Carbide/Carbon Composites Synthesized by a Microwave Heating method as Supports of Platinum Catalysts for Methanol Oxidation. *J. Power Sources* **2012**, *202*, 56–62.
32. Du, D. J.; Cao, M. H.; He, X. Y.; Liu, Y. Y.; Hu, C. W. Morphology-Controllable Synthesis of Microporous Prussian Blue Analogue $Zn_3[Co(CN)_6]_2 \cdot xH_2O$ Microstructures. *Langmuir* **2009**, *25*, 7057–7062.
33. Srinivas, G.; Krungleviciute, V.; Guo, Z. X.; Yildirim, T. Exceptional CO_2 Capture in a Hierarchically Porous Carbon with Simultaneous High Surface Area and Pore Volume. *Energy Environ. Sci.* **2014**, *7*, 335–342.
34. Huang, W.; Wang, Y.; Luo, G. H.; Wei, F. 99.9% Purity Multi-Walled Carbon Nanotubes by Vacuum High-Temperature Annealing. *Carbon* **2003**, *41*, 2585–2590.

35. Zhang, L.; Wu, H. B.; Madhavi, S.; Hng, H. H.; Lou, X. W. Formation of Fe_2O_3 Microboxes with Hierarchical Shell Structures from Metal−Organic Frameworks and Their Lithium Storage Properties. *J. Am. Chem. Soc.* **2012**, *134*, 17388–17391.
36. Yang, S. J.; Nam, S.; Kim, T.; Im, J. H.; Jung, H.; Kang, J. H.; Wi, S. G.; Park, B.; Park, C. R. Preparation and Exceptional Lithium Anodic Performance of Porous Carbon-Coated ZnO Quantum Dots Derived from a Metal−Organic Framework. *J. Am. Chem. Soc.* **2013**, *135*, 7394–7397.
37. Yan, N.; Wang, F.; Zhong, H.; Li, Y.; Wang, Y.; Hu, L.; Chen, Q. W. Hollow Porous SiO_2 Nanocubes Towards High-performance Anodes for Lithium-ion Batteries. *Sci. Rep.* **2013**, *3*, 1568–1573.
38. Xiao, Y.; Cao, M. H.; Ren, L.; Hu, C. W. Hierarchically Porous Germanium-Modified Carbon Materials with Enhanced Lithium Storage Performance. *Nanoscale* **2012**, *4*, 7469–7474.
39. Liu, H.; Su, D. W.; Zhou, R. F.; Sun, B.; Wang, G. X.; Qiao, S. Z. Highly Ordered Mesoporous MoS_2 with Expanded Spacing of the (002) Crystal Plane for Ultrafast Lithium Ion Storage. *Adv. Energy Mater.* **2012**, *2*, 970–975.
40. Zhang, L.; Wu, H. B.; Madhavi, S.; Hug, H. H.; Lou, X. W. Metal-Organic-Frameworks-Derived General Formation of Hollow Structures with High Complexity. *J. Am. Chem. Soc.* **2013**, *135*, 10664–10672.
41. Li, Z.; Xu, Z. W.; Tan, X. H.; Wang, H. L.; Holt, C. M. B.; Stephenson, T.; Olsen, B. C.; Mitlin, D. Mesoporous Nitrogen-Rich Carbons Derived from Protein for Ultra-High Capacity Battery Anodes and Supercapacitors. *Energy Environ. Sci.* **2013**, *6*, 871–878.
42. Mukherjee, R.; Thomas, A. V.; Datta, D.; Singh, E.; Li, J. W.; Eksik, O.; Shenoy, V. B.; Koratkar, N. Defect-Induced Plating of Lithium Metal within Porous Graphene Networks. *Nat. Commun.* **2014**, *5*, 3710–3719.
43. Mahmood, N.; Zhang, C. Z.; Liu, F.; Zhu, J. H.; Hou, Y. L. Hybrid of Co_3Sn_2@Co Nanoparticles and Nitrogen-Doped Graphene as a Lithium Ion Battery Anode. *ACS Nano* **2013**, *7*, 10307–10318.
44. Wang, B.; Li, X. L.; Qiu, T. F.; Luo, B.; Ning, J.; Li, J.; Zhang, X. F.; Liang, M. H.; Zhi, L. J. High Volumetric Capacity Silicon-Based Lithium Battery Anodes by Nanoscale System Engineering. *Nano Lett.* **2013**, *13*, 5578–5584.
45. Wu, Z. S.; Yang, S.; Sun, Y.; Wu, Z. S.; Yang, S.; Sun, Y.; Parvez, K.; Feng, X.; Müllen, K. 3D Nitrogen-Doped Graphene Aerogel-Supported Fe_3O_4 Nanoparticles as Efficient Electrocatalysts for the Oxygen Reduction Reaction. *J. Am. Chem. Soc.* **2012**, *134*, 9082–9085.
46. Wu, Z. S.; Ren, W.; Xu, L.; Li, F.; Cheng, H. M. Doped Graphene Sheets as Anode Materials with Superhigh Rate and Large Capacity for Lithium Ion Batteries. *ACS Nano* **2011**, *5*, 5463–5471.
47. Xia, Y.; Xiao, Z.; Dou, X.; Huang, H.; Lu, X. H.; Yan, R. J.; Gan, Y. P.; Zhu, W. J.; Tu, J. P.; Zhang, W. K.; Tao, X. Y. Green and Facile Fabrication of Hollow Porous MnO/C Microspheres from Microalgaes for Lithium-Ion Batteries. *ACS Nano* **2013**, *7*, 7083–7092.
48. Wang, J.; Zhou, Y. K.; Hu, Y. Y.; O'Hayre, R.; Shao, Z. P. Porous Nanocrystalline TiO_2 with High Lithium-Ion Insertion Performance. *J. Mater. Sci.* **2013**, *48*, 2733–2742.
49. Xia, Y.; Zhang, W. K.; Huang, H.; Gan, Y. P.; Xiao, Z.; Qian, L. C.; Tao, X. Y. Biotemplating of Phosphate Hierarchical Rechargeable $LiFePO_4$/C Spirulina Microstructures. *J. Mater. Chem.* **2011**, *21*, 6498–6501.
50. Wang, C.; Wan, W.; Huang, Y. H.; Chen, J. T.; Zhou, H. H.; Zhang, X. X. Hierarchical MoS_2 Nanosheet/Active Carbon Fiber Cloth as a Binder-Free and Free-Standing Anode for Lithium-Ion Batteries. *Nanoscale* **2014**, *6*, 5351–5358.
51. Shin, J.; Ryu, W. H.; Park, K. S.; Kim, I. D. Morphological Evolution of Carbon Nanofibers Encapsulating SnCo Alloys and Its Effect on Growth of the Solid Electrolyte Interphase Layer. *ACS Nano* **2013**, *7*, 7330–7341.
52. Rong, J. P.; Masarapu, C. R.; Ni, J.; Zhang, Z. J.; Wei, B. Q. Tandem Structure of Porous Silicon Film on Single-Walled Carbon Nanotube Macrofilms for Lithium-Ion Battery Applications. *ACS Nano* **2010**, *4*, 4683–4690.
53. Qin, J.; He, C. N.; Zhao, N.; Wang, Q.; Shi, Z. Y.; Liu, C. S.; Li, E. Z.; Graphene, J. J. Networks Anchored with Sn@Graphene as Lithium Ion Battery Anode. *ACS Nano* **2014**, *8*, 1728–1738.
54. Tian, L. L.; Wei, X. Y.; Zhuang, Q. C.; Jiang, C. H.; Wu, C.; Ma, G. Y.; Zhao, X.; Zong, Z. M.; Sun, S. G. Bottom-Up Synthesis of Nitrogen-Doped Graphene Sheets for Ultrafast Lithium Storage. *Nanoscale* **2014**, *6*, 6075–6083.
55. Zhu, Z. Q.; Wang, S. W.; Du, J.; Jin, Q.; Zhang, T. R.; Cheng, F. Y.; Chen, J. Ultrasmall Sn Nanoparticles Embedded in Nitrogen-Doped Porous Carbon as High-Performance Anode for Lithium-Ion Batteries. *Nano Lett.* **2014**, *14*, 153–157.
56. Wu, Z. S.; Ren, W. C.; Wen, L.; Gao, L. B.; Zhao, J. P.; Chen, Z. P.; Zhou, G. M.; Li, F.; Cheng, H. M. Graphene Anchored with Co_3O_4 Nanoparticles as Anode of Lithium Ion Batteries with Enhanced Reversible Capacity and Cyclic Performance. *ACS Nano* **2010**, *4*, 3187–3194.